An Emissivity-Based Wind Vector Retrieval Algorithm for the WindSat Polarimetric Radiometer

Shannon T. Brown, *Member IEEE*, Christopher S. Ruf, *Fellow, IEEE*, and David R. Lyzenga

***Abstract*—The Naval Research Laboratory WindSat polarimetric radiometer was launched on January 6, 2003 and is the first fully polarimetric radiometer to be flown in space. WindSat has three fully polarimetric channels at 10.7, 18.7, and 37.0 GHz and vertically and horizontally polarized channels at 6.8 and 23.8 GHz. A first-generation wind vector retrieval algorithm for the WindSat polarimetric radiometer is developed in this study. An atmospheric clearing algorithm is used to estimate the surface emissivity from the measured WindSat brightness temperature at each channel. A specular correction factor is introduced in the radiative transfer equation to account for excess reflected atmospheric brightness, compared to the specular assumption, as a function wind speed. An empirical geophysical model function relating the surface emissivity to the wind vector is derived using coincident QuikSCAT scatterometer wind vector measurements. The confidence in the derived harmonics for the polarimetric channels is high and should be considered suitable to validate analytical surface scattering models for polarized ocean surface emission. The performance of the retrieval algorithm is assessed with comparisons to Global Data Assimilation System (GDAS) wind vector outputs. The root mean square (RMS) uncertainty of the closest wind direction ambiguity is less than 20° for wind speeds greater than 6 m/s and less than 15° at 10 m/s and greater. The retrieval skill, the percentage of retrievals in which the first-rank solution is the closest to the GDAS reference, is 75% at 7 m/s and 85% or higher above 10 m/s. The wind speed is retrieved with an RMS uncertainty of 1.5 m/s.**

***Index Terms*—Polarimetry, sea surface emissivity, wind vector, WindSat.**

I. Introduction

INVESTIGATIONS of the use of polarimetric microwave radiometers to retrieve the wind vector (speed and direction) over the ocean began in the early 1990s with highly successful proof of concept aircraft experiments [1]–[3] and has culminated with the launch of the Naval Research Laboratory (NRL) WindSat polarimetric radiometer in 2003. WindSat is the first fully polarimetric radiometer to be flown in space and serves as risk mitigation for the next-generation NPOESS Conically Scanning Microwave Imager/Sounder (CMIS). It was launched on January 6, 2003 on the Department of Defense's Coriolis satellite. A complete instrument description can be found in [4]. WindSat measures all four components of the modified Stokes vector [5] at 10.7, 18.7, and 37.0 GHz. The modified Stokes vector is defined as

$$I_s = \begin{bmatrix} T_V \\ T_H \\ U \\ V \end{bmatrix} = \begin{bmatrix} T_V \\ T_H \\ T_{+45} - T_{-45} \\ T_{lc} - T_{rc} \end{bmatrix} = \frac{\lambda^2}{k_B \eta} \begin{bmatrix} \langle E_V E_V^* \rangle \\ \langle E_H E_H^* \rangle \\ 2\mathrm{Re}\,\langle E_V E_H^* \rangle \\ 2\mathrm{Im}\,\langle E_V E_H^* \rangle \end{bmatrix} \quad (1)$$

where T_V and T_H are the vertically and horizontally polarized brightness temperatures (T_B), T_{+45} and T_{-45} are the $+45°$ and $-45°$ slant linear polarized T_Bs and T_{lc} and T_{rc} are the left hand and right hand circular polarized T_Bs. WindSat also has two additional channels at 6.8 and 23.8 GHz for which only the vertically and horizontally polarized T_B is measured. The combination of these channels provides an unprecedented opportunity to produce passive microwave retrievals of the ocean surface wind vector from space. In order to retrieve the ocean surface wind vector, a geophysical forward model is needed relating the sea surface emissivity to the wind speed and direction. Analytical surface scattering models have been able to predict some of the observed polarimetric emission characteristics of an ocean surface modified by wind [6]–[8]. Yet these models remain an approximation for the complex physics involved and suffer from modeling uncertainties such as the treatment of the sea spectrum and the effect of foaming and white caps and thus are not able to fully predict the observed behavior of the wind induced sea surface emission. Therefore, the use of an empirical geophysical model function (GMF) derived from polarimetric radiometer observations is seen as a reasonable candidate to serve as the forward model in the wind vector retrieval algorithm. In this study, an empirical GMF is derived relating the polarimetric sea surface emissivity to the near surface wind vector. The surface emissivity is determined from the measured WindSat brightness temperatures using an atmospheric clearing algorithm developed in Section II. A Fourier expansion is used to represent the dependence of the surface emissivity on wind vector where the Fourier harmonic coefficients are determined from WindSat emissivity measurements colocated with NASA QuikSCAT scatterometer measurements of the surface wind vector. A wind vector retrieval algorithm is developed in Section IV using the empirical GMF. The performance of the retrieval algorithm is assessed in Section V from comparisons with wind vector outputs from the National Centers for Environmental Prediction (NCEP) Global Data Assimilation System (GDAS). The wind vector, for both QuikSCAT and GDAS, is referenced

Manuscript received February 2, 2005; revised August 10, 2005.
S. T. Brown is with the Micrwoave Advanced Systems, Jet Propulsion Laboratory, Pasadena, CA 91109 USA (e-mail: shannon.t.brown@jpl.nasa.gov).
C. S. Ruff is with the Space Physics Research Laboratory, Department of Atmospheric, Oceanic, and Space Sciences, University of Michigan, Ann Arbor, 48109 MI USA.
D. R. Lyzenga is with the Department of Naval Architecture and Marine Engineering, University of Michigan, Ann Arbor, MI 48109-2145 USA.
Digital Object Identifier 10.1109/TGRS.2005.859351

to a height of 10 m. All WindSat data used in this paper were processed using version 1.6.1 of the WindSat ground data processing software. Only WindSat data from the fore scan were used and an along scan calibration bias correction provided for the 1.6.1 data was applied to all channels.

II. Atmospheric Clearing Algorithm

A. Methodology

The surface emissivity can be estimated from brightness temperature measurements provided that the contribution from the atmosphere is estimated and removed. The measured brightness temperature for a given WindSat channel is a function of the emission from the atmosphere and the surface, which can be represented by the radiative transfer equation [9]

$$T_B(f,p,\theta) = \varepsilon(f,p,\theta)T_{\mathrm{surf}}e^{-\tau(f)\sec\theta} + T_{\mathrm{UP}}(f,\theta) + \Gamma\left(T_{\mathrm{DOWN}}(f,\theta) + T_{\cos mic}e^{-\tau(f)\sec\theta}\right)e^{-\tau(f)\sec\theta} \quad (2)$$

where

- T_B measured brightness temperature;
- θ incidence angle;
- f frequency;
- p polarization;
- T_{surf} sea surface temperature (K);
- ε surface emissivity;
- T_{UP} atmospheric upwelling brightness surface reflectivity temperature;
- T_{DOWN} atmospheric downwelling brightness temperature;
- T_{cosmic} cosmic background brightness temperature;
- $\tau(f)$ zenith integrated atmospheric optical depth as a function of frequency;
- Γ surface reflectivity.

Equation (2) assumes a nonscattering atmosphere which is valid for rain-free pixels. The upwelling and downwelling atmospheric brightness temperatures in (2) can be approximated as a function of the optical depth

$$T_{\mathrm{UP}}(f,\theta) = \left(1 - e^{-\tau(f)\sec\theta}\right)T_{\mathrm{eff}}^{\mathrm{UP}}(f, \mathrm{Latitude}) \quad (3a)$$

$$T_{\mathrm{DOWN}}(f,\theta) = \left(1 - e^{-\tau(f)\sec\theta}\right)T_{\mathrm{eff}}^{\mathrm{DOWN}}(f, \mathrm{Latitude}) \quad (3b)$$

where $T_{\mathrm{eff}}^{\mathrm{UP}}$ and $T_{\mathrm{eff}}^{\mathrm{DOWN}}$ are latitude-dependent atmospheric effective radiating temperatures to be determined. This atmospheric model for T_{UP} and T_{DOWN} has been shown to be a good approximation to the complete integral solution [10], which would require knowledge of the actual atmospheric profile of temperature, pressure, water vapor and cloud liquid water. The optical depth of a nonraining atmosphere for a given frequency can be expressed with high accuracy as a polynomial function of the integrated water vapor (V) in centimeters and cloud liquid water (L) in millimeters

$$\tau(f) = c_{0,f} + c_{1,f}V + c_{2,f}V^2 + c_{3,f}L + c_{4.f}L^2 \quad (4)$$

TABLE I
Frequency-Dependent c Coefficients Used in (4) That Relate the Optical Depth to the Integrated Water Vapor and Cloud Liquid Water Content of the Atmosphere

Equation (2)	6.8 GHz	10.7 GHz	18.7 GHz	23.8 GHz	37.0 GHz
c_0	1.039e-2	1.184e-2	1.742e-2	2.593e-2	7.081e-2
$c_1\ (\mathrm{cm})^{-1}$	-3.576e-5	8.040e-4	1.571e-2	4.748e-2	7.440e-3
$c_2\ (\mathrm{cm})^{-2}$	3.993e-5	4.720e-5	-8.476e-6	5.630e-4	5.135e-4
$c_3\ (\mathrm{mm})^{-1}$	6.788e-3	1.540e-2	4.539e-2	7.086e-2	1.709e-1
$c_4\ (\mathrm{mm})^{-2}$	-2.121e-3	-4.202e-3	-1.348e-2	-1.194e-2	-4.609e-2

TABLE II
Upwelling Atmosphere Effective Radiating Temperature Used in (3a). Values Are Given in 10° Latitude Increments and Are Assumed Symmetric With Latitude

Upwelling T_{eff}(Latitude) (K)	6.8 GHz	10.7 GHz	18.7 GHz	23.8 GHz	37.0 GHz
0°-10°	275.12	278.48	285.52	284.80	277.67
10°-20°	274.10	277.15	284.67	284.64	276.40
20°-30°	271.15	273.50	280.58	280.77	272.26
30°-40°	267.50	269.41	277.11	278.30	267.85
40°-50°	260.12	260.97	267.02	268.87	258.81
50°-60°	254.06	254.39	258.70	260.46	252.34

where the frequency-dependent coefficients are determined by a regression analysis (described below). Equations (2)–(4) parameterize the T_B observations in terms of V, L and surface emissivity, which are retrieved by a least squares procedure.

B. Parameterization of the Atmospheric Model

The regression coefficients in (4), and the effective radiating temperatures in (3a) and (3b) must be determined at each WindSat frequency. A plane parallel radiative transfer model is used with globally distributed radiosonde profiles (RaObs) in order to estimate the integrated atmospheric optical depth and the upwelling and downwelling T_Bs. RaOb sounding data at 56 open-ocean island launch sites from October 2001 through September 2002 ($\sim$ 22 000 profiles) are used in the model. The radiosonde data are acquired from NOAA's Forecast Systems Laboratory (FSL) radiosonde database.

The atmospheric gaseous absorption is determined using the oxygen absorption model of [11] and an updated version of the Liebe water vapor absorption model [12]. A model from [13] is used to estimate the amount of cloud liquid water present in each radiosonde profile. The cloud liquid water absorption model is from [14].

The regression coefficients in (4) are determined using a least squares fit of the integrated vapor and cloud liquid to the modeled optical depth at each frequency. They are listed in Table I. The upwelling and downwelling effective radiating temperatures are determined using (3a) and (3b) together with the atmospheric upwelling and downwelling T_Bs and optical depth determined from the radiative transfer model and are taken to be the average over the entire model dataset in 10° latitude increments. The effective radiating temperatures are assumed symmetric with latitude. They are listed in Tables II and III. In the algorithm, a cubic spline interpolation of the values in Tables II and III is used to determine the effective radiating temperature at intermediate values of latitude.

TABLE III
DOWNWELLING ATMOSPHERE EFFECTIVE RADIATING TEMPERATURE USED IN (3b). VALUES ARE GIVEN IN 10° LATITUDE INCREMENTS AND ARE ASSUMED SYMMETRIC WITH LATITUDE

Downwelling T_{eff}(Latitude) (K)	6.8 GHz	10.7 GHz	18.7 GHz	23.8 GHz	37.0 GHz
0°-10°	275.37	278.80	286.73	287.78	280.23
10°-20°	274.33	277.45	285.68	286.99	278.69
20°-30°	271.37	273.78	281.52	282.97	274.39
30°-40°	267.72	269.67	277.93	280.03	269.83
40°-50°	260.30	261.20	267.63	270.04	260.49
50°-60°	254.23	254.59	259.20	261.38	253.74

TABLE IV
VALUES FOR THE SPECULAR CORRECTION FACTOR IN (5) AT 8 AND 16 m/s FOR ALL WINDSAT CHANNELS

f(GHz)	WS(m/s)	V	H	+45	-45	LCP	RCP
6.8	8	1.145	1.323	1.253	1.255	1.254	1.254
6.8	16	1.206	1.487	1.374	1.380	1.377	1.377
10.7	8	1.152	1.300	1.239	1.242	1.241	1.241
10.7	16	1.234	1.484	1.379	1.388	1.384	1.383
18.7	8	1.107	1.334	1.251	1.254	1.253	1.253
18.7	16	1.131	1.461	1.334	1.343	1.339	1.339
23.8	8	1.074	1.232	1.173	1.175	1.174	1.174
23.8	16	1.091	1.320	1.230	1.237	1.234	1.234
37.0	8	1.135	1.420	1.320	1.324	1.322	1.322
37.0	16	1.196	1.619	1.461	1.472	1.467	1.466

C. Estimating Atmospheric Water Vapor and Cloud Liquid Water

Equations (2)–(4) present a set of simultaneous equations for WindSat T_B measurements as functions of surface emissivity, V and L. This requires a simultaneous solution for the emissivity, water vapor and cloud liquid water. The solution is found in two steps. The first step is intended to retrieve V and L. Only V-pol channels are used in order to reduce the sensitivity of the solution for V and L to wind speed and direction. Surface emissivity is also retrieved in the first step, but only as a secondary parameter. For this reason, a simplified surface emission model is used that does not depend on wind direction. The emission model given by [15] is used and the excess emission due to surface roughness and sea foam is modeled using [16]. Seasonally dependent climatological values for the sea surface salinity in a $1° \times 1°$ latitude/longitude grid from NOAA [17] are used. The sea surface temperature is taken from GDAS outputs, which were less than 3 h apart from the WindSat measurement. The three unknowns, V, L, and WS, are solved for using an iterative Newton–Raphson method [18] with the colocated 10.7-, 18.7-, 23.8-, and 37.0-GHz vertically polarized WindSat T_B measurements. The 6.8-GHz channel was not included due to calibration problems at the time of the study, but will be applied in future versions of the algorithm to estimate the SST along with the other unknowns. The value of the wind speed determined here is not used in the second stage of processing (using other polarization channels) that retrieves wind direction. Once V and L are determined, the optical depth and atmospheric upwelling and downwelling are known for all WindSat channels. This allows the surface emissivity at each WindSat channel to be estimated by inverting (2). The emissivities are then used with colocated QuikSCAT wind vector measurements to parameterize the empirical GMF discussed in Section III.

D. Nonspecular Downwelling Correction

For a specular ocean surface, the power reflectivity, Γ, can be expressed as $1 - \varepsilon$. This specular condition is only strictly valid for a perfectly flat ocean surface, although it is assumed in many radiometric retrieval algorithms for wind roughened ocean surfaces. The reflected downwelling brightness for a slightly roughened ocean surface will largely originate from the specular direction, but as the surface roughness increases (i.e., wind speed increases) a larger amount of reflected energy will originate at angles of incidence that are larger and smaller than the specular direction. The net effect of this will cause the true reflected downwelling brightness to increase from the specular value since the atmospheric brightness scales with the secant of the incidence angle. A more accurate representation for the ocean surface reflectivity is to use a rigorous analytical model, such as the two-scale model [6], [19], [20] to calculate the bistatic scattering coefficient for all scattering angles in order to determine the hemispherically integrated reflected brightness. Incorporating a full analytical model for the surface power reflectivity into the retrieval algorithm would be computationally prohibitive. Therefore, the specular condition is assumed and a correction factor, Ω, representing the ratio of the "true" reflectivity to the specular reflectivity, is added. A correction of this form was first proposed by [21] and has subsequently been used by several authors for microwave radiative transfer calculations. Here, the "true" reflectivity is taken to be the reflected brightness determined using the full two-scale model [22] and Ω is simply the ratio of that to specular reflected brightness

$$\begin{aligned}\Gamma T_{\text{sky}}(\theta) &= \Omega\,(1-\varepsilon)\,T_{\text{sky}}(\theta)\\ &= \frac{1}{4\pi}\int\!\!\int T_{\text{sky}}(\theta_s,\phi_s)\gamma(\theta,\phi,\theta_s,\phi_s)\sin\theta_s d\theta_s d\phi_s\end{aligned} \tag{5}$$

where T_{sky} includes contributions from the atmosphere and cosmic background, (θ, ϕ) is the viewing direction of the radiometer, (θ_s, ϕ_s) is the scattering direction, and γ is the bistatic scattering coefficient.

The value of Ω is dependent on the wind speed and direction, and on the atmospheric conditions, such as the water vapor and cloud liquid water concentration, although the latter dependence is expected to be small for the third and fourth Stokes parameters. In this study, Ω is assumed to vary with wind speed only and is taken to be the average value over all wind directions for a given wind speed. Neglecting the directional and atmospheric dependence of Ω is not expected to have a large impact on the retrieval since the correction factor itself is small. However, future investigations will include these additional dependencies of Ω. To model its dependence on wind speed, Ω is computed at 8 and 16 m/s for each WindSat frequency and polarization and a linear fit is used to extrapolate/interpolate the values at other wind speeds. Values are given in Table IV. It should be noted that sea foam is not represented in the two-scale model used to calculate the "true" reflected brightness. Therefore, this simple linear model will overestimate Ω at high wind speeds when the foam covered fraction of the footprint becomes appreciable. This is because sea foam acts nearly as a blackbody absorber, meaning only the foam free fraction of the footprint will contribute to the reflected brightness temperature. Future improvements to the model will include a representation for sea foam in the determination of Ω, as well as a more accurate parameterization of the foam-free reflectivity.

III. Empirical Geophysical Model Function

A geophysical model function is developed that relates the surface emissivity at each frequency and polarization to the wind speed and direction. Previous ocean surface emission models and aircraft radiometer observations have determined that the vertical and horizontal surface emissivity is an even function of the relative wind direction and the third and fourth stokes emissivity is as an odd function of the relative wind direction [1], [2], [20]. The emissivity can therefore be expanded as an even or odd Fourier series, respectively. Expanding the series to the second harmonic gives

$$\varepsilon_{V,H}(\mathrm{WS}, \phi, \mathrm{SST}) = a_0(\mathrm{WS}, \mathrm{SST}, \theta) + a_1(\mathrm{WS}) \cos \phi + a_2(\mathrm{WS}) \cos 2\phi, \quad (6a)$$

$$\varepsilon_{3,4}(\mathrm{WS}, \phi) = b_0 + b_1(\mathrm{WS}) \sin \phi + b_2(\mathrm{WS}) \sin 2\phi \quad (6b)$$

where $\phi = \phi_R - \phi_W$ is the angle between the look direction of the radiometer, ϕ_R, and the direction the wind is blowing from, ϕ_W. ϕ_W is referenced to the compass with 0° as north and 90° as east. A relative direction of 0° is generally referred to as the upwind direction, i.e., with the wind blowing toward the radiometer. It should be noted that the definition of the relative wind direction, ϕ, used here is equivalent to that used in previous work [2], [6]. Although, in both [2] and [6] the relative wind direction is defined as $\phi_W - \phi_R$, but the angle is measured counterclockwise from the x axis (north), whereas here it is measured clockwise, using the geographical convention. The coefficients in (6) are functions of wind speed, sea surface temperature and salinity, swell, incidence angle, frequency, and polarization [6]. The first- and second-order harmonic coefficients have a first-order dependence on the surface wind speed. The dependence of these coefficients on other environmental parameters such as the salinity and air–sea temperature difference is generally much weaker. They are, therefore, assumed to vary only with wind speed for a given channel. As long-term global polarimetric data sets become available, these second-order dependencies can be investigated further.

The zeroth-order harmonics for V- and H-pol should increase monotonically with wind speed and reduce to the specular emissivity as the wind speed approaches zero. An empirical relation is derived that relates the V- and H-pol zeroth harmonic to the surface wind speed, SST, and incidence angle. The relation is of the form

$$a_0 = d_0 + d_1\theta + d_2\mathrm{WS} + d_3\mathrm{WS}^2 + d_4\mathrm{SST} \quad \text{for WS} \le 7 \quad (7a)$$

$$a_0 = e_0 + e_1\theta + e_2\mathrm{WS} + e_3\mathrm{WS}^2 + e_4\mathrm{WS}^3 + e_5\mathrm{SST} \quad \text{for WS} > 7 \quad (7b)$$

wher SST is in Kelvin, WS is in meters per second, and θ is in degrees. Incidence angle is included in the empirical relation because a slight misalignment of the spin axis for the conical scan causes a variation in incidence angle of approximately 1° about the nominal value over a complete azimuth rotation. The zeroth-order harmonic for the third and the fourth stokes parameters is generally thought be zero for the ocean surface [3], [6], but a nonzero component is included here to account for calibration offsets of the radiometer. The coefficients in (6) and (7) are estimated using measured WindSat emissivities colocated with QuikSCAT measurements of the wind speed and direction and together with GDAS outputs for the SST.

TABLE V
Coefficients for the V- and H-Pol Zeroth Harmonic Empirical Formula for Wind Speeds ≤ 7 m/s, (7a)

Zeroth-order Coefficients (7a)	10.7 V	10.7 H	18.7 V	18.7 H	37.0 V	37.0 H
d_0	-0.5532	0.168	-0.415	0.358	0.649	1.521
d_1 (degree)$^{-1}$	0.0117	-3.23e-3	1.236e-2	-3.776e-3	4.035e-3	-1.736e-2
d_2 (m/s)$^{-1}$	1.1690e-4	2.614e-3	-2.286e-4	5.272e-3	5.379e-4	4.807e-3
d_3 (m/s)$^{-2}$	0.0	-8.21e-5	0.0	-1.652e-4	0.0	0.0
d_4 (K)$^{-1}$	1.662e-3	9.137e-4	1.12e-3	3.759e-4	-8.345e-4	-9.586e-4

TABLE VI
Coefficients for the V- and H-Pol Zeroth Harmonic Empirical Formula for Wind Speeds > 7 m/s, (7b)

Zeroth-order Coefficients (7b)	10.7 V	10.7 H	18.7 V	18.7 H	37.0 V	37.0 H
e_0	-0.214	6.395e-2	0.355	0.543	0.719	0.823
e_1 (degree)$^{-1}$	8.459e-3	1.976e-3	2.497e-3	-2.007e-3	4.469e-3	-5.897e-4
e_2 (m/s)$^{-1}$	-5.348e-3	-7.362e-3	-7.500e-3	-1.376e-2	-1.346e-2	-1.789e-2
e_3 (m/s)$^{-2}$	5.310e-4	7.724e-4	7.172e-4	1.421e-3	-1.346e-2	1.686e-3
e_4 (m/s)$^{-3}$	-1.193e-5	-1.783e-5	-1.641e-5	-3.335e-5	-2.590e-5	-3.793e-5
e_5 (K)$^{-1}$	1.121e-3	5.035e-4	4.586e-4	-3.483e-4	-9.862e-4	-1.331e-3

WindSat emissivities are determined from (2) using the atmospheric clearing algorithm described above. A six month data base of WindSat measurements colocated with QuikSCAT wind vector retrievals was provided to the WindSat science team by NRL. Several quality control filters were used on the colocated dataset in order to ensure the quality of the estimates of the harmonic coefficients. The spatial and temporal separation between the QuikSCAT and WindSat measurements was not allowed to exceed 7 km and 1 min for wind speeds less than 15 m/s; 25 km and 10 min for wind speeds greater than 15 m/s and less than 20 m/s; 25 km and 15 min for wind speeds greater than 20 m/s and less than 30 m/s; and 25 km and 60 min for wind speeds greater than 30 m/s. The integrated cloud liquid water, as determined from the WindSat brightness temperatures using the algorithm described in Section II, was not allowed to exceed 0.3 mm, which eliminated most rain data. Both the retrieved integrated water vapor and the surface emissivity were required to be physical, 0 to 7 cm and 0 to 1, respectively, although very few points failed to satisfy these requirements. The filtered dataset consisted of approximately 150 000 globally distributed match-ups over a wide range of wind speeds and directions, sea surface temperatures and atmospheric conditions. The QuikSCAT match-ups are stratified into 1-m/s bins and a least-squares regression is used to determine the harmonic coefficients as a function of frequency, polarization and wind speed. The resulting coefficients in (7) are adjusted to remove any discontinuity at a wind speed of 7 m/s. The coefficients are listed in Tables V and VI. The first- and second-order harmonic coefficients as a function of wind speed for the third and fourth stokes

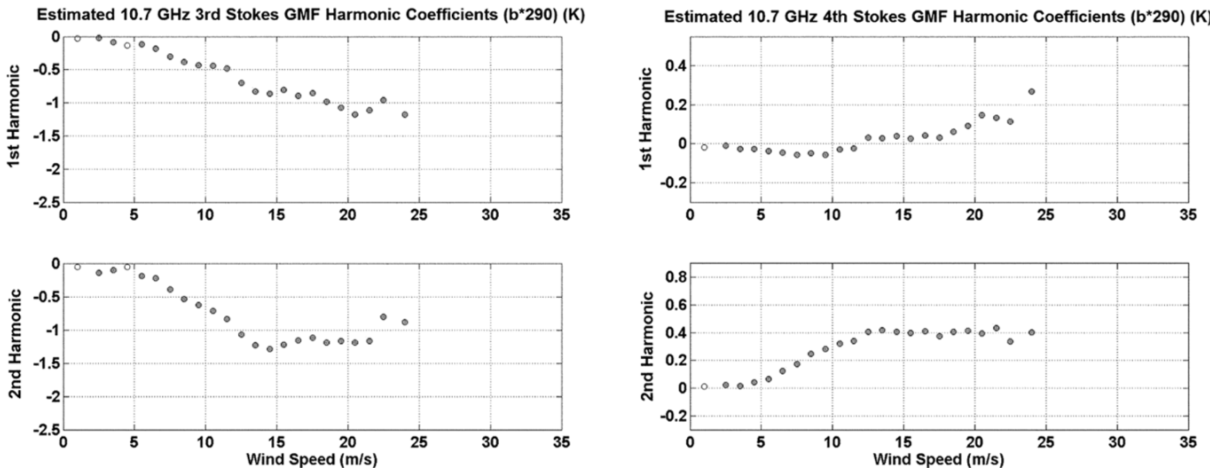

Fig. 1. The 10.7-GHz first and second harmonic coefficients as a function of wind speed estimated from the WindSat 10.7-GHz (left) third and (right) fourth Stokes channels.

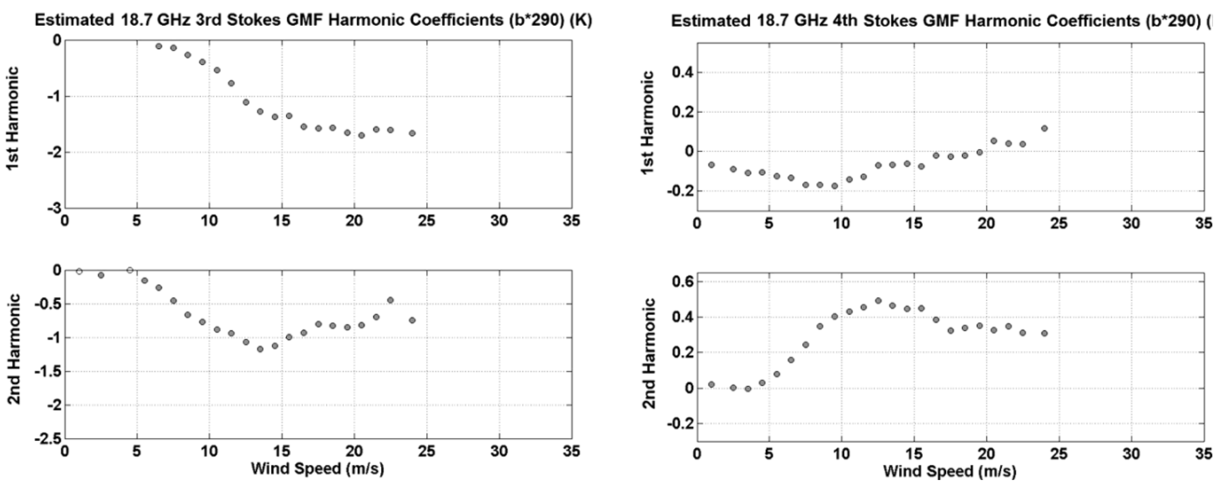

Fig. 2. The 18.7-GHz first and second harmonic coefficients as a function of wind speed estimated from the WindSat 18.7-GHz (left) third and (right) fourth Stokes channels.

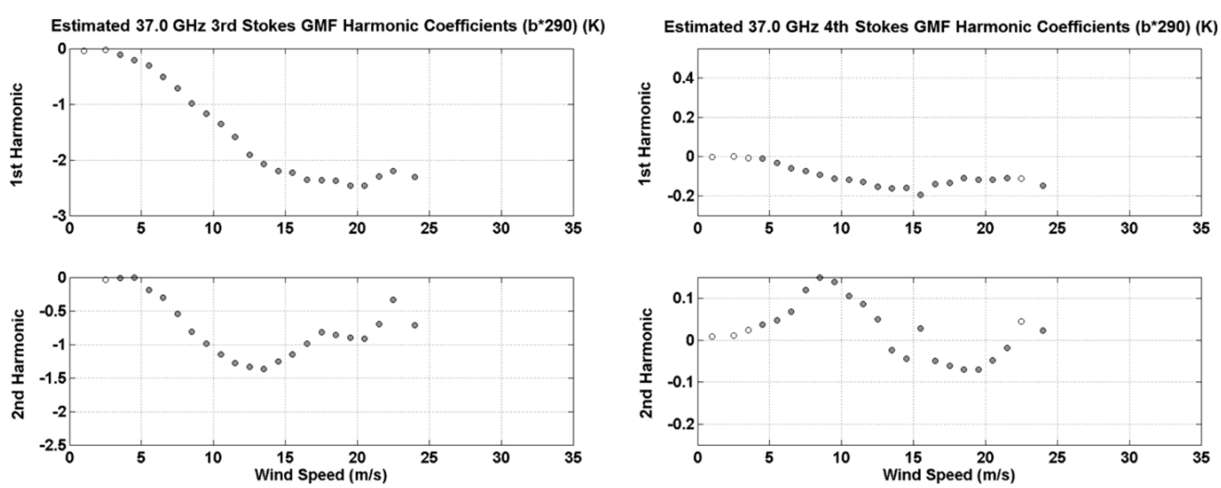

Fig. 3. The 37.0-GHz first and second harmonic coefficients as a function of wind speed estimated from the WindSat 37.0-GHz (left) third and (right) fourth Stokes channels.

are shown in Figs. 1–3 for 10.7, 18.7, and 37.0 GHz, scaled to values of surface brightness temperature ($\varepsilon * 290$ K).

The correlation coefficient of the harmonic fits for the third and fourth stokes emissivities was routinely greater than 0.95 for wind speeds greater than 5 m/s and less than 20 m/s. The confidence of the harmonic fit was lower for wind speeds less than 5 m/s due to the weak signal strength of the emission approaching the noise floor of the emissivity retrieval. The confidence also degraded for wind speeds greater than 20 m/s due to a decrease in the data volume over all relative wind directions. Due to the high confidence in the estimates for the harmonic coefficients over the range of 5–20 m/s, an interpolation

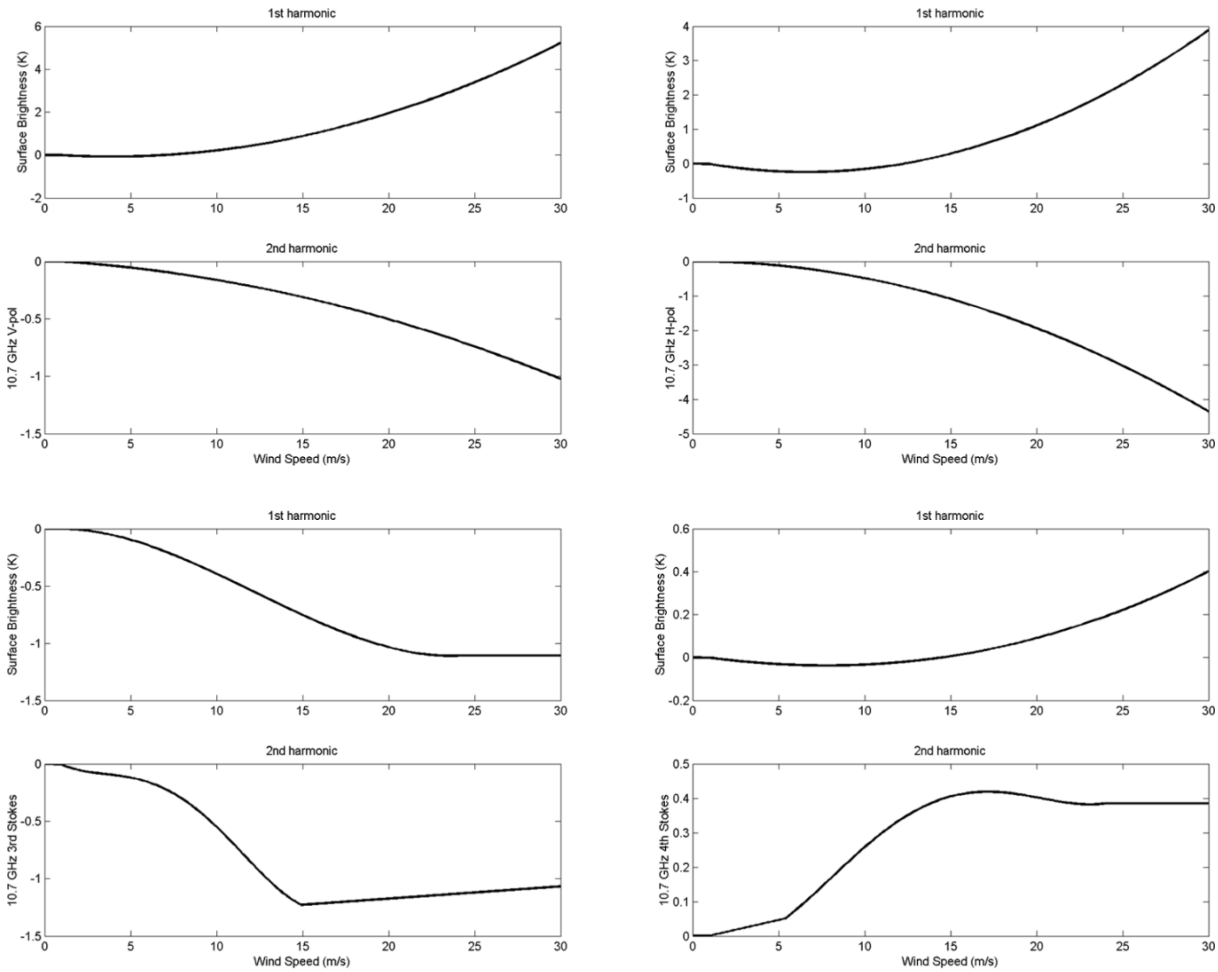

Fig. 4. The 10.7-GHz V (top left), H (top right), third (bottom left), and fourth (bottom right) Stokes first and second harmonic coefficients estimated from WindSat scaled to surface brightness ($\varepsilon * 290$) (K). The coefficients are interpolated/extrapolated from the WindSat data, shown for the third and fourth stokes in Fig. 1.

was used to determine the harmonic coefficients as a function of wind speed in 0.1-m/s steps over this range. Polynomial fits were used to extrapolate the harmonics for wind speeds less than 5 m/s and greater than 20 m/s. The estimated harmonic coefficients for each channel were placed in a look up table for wind speeds between 0 and 30 m/s in 0.1-m/s increments. The estimated first and second harmonic coefficients for each channel are shown in Figs. 4–6.

The magnitude of the third stokes first harmonic is observed to increase with wind speed and frequency. Saturation features are observed in the first harmonic at all frequencies and are most prevalent in the 37.0-GHz channel. Saturation begins around 15 m/s at 18.7 and 37.0 GHz and near 20 m/s for the 10.7-GHz channel. The magnitude of the third stokes second harmonic also increases with wind speed and appears to be independent of frequency for wind speeds less than 13 m/s. The maximum absolute value of the second harmonic is observed at 13–14 m/s for all frequencies. The signal then levels off with increasing wind speed at 10.7 GHz and tends toward zero at 18.7 and 37.0 GHz.

The fourth stokes first harmonic is small for all frequencies and almost negligible at 10.7 GHz. The 10.7- and 18.7-GHz first harmonic is observed to decrease slightly with wind speed to 10 m/s, at which point the slope reverses and the signal increases with wind speed. The 37.0-GHz first harmonic decreases with wind speed to 15 m/s and then saturates. The fourth stokes second harmonic is not observed below 5 m/s at 10.7 and 18.7 GHz. At 5 m/s the signal is observed to increase rapidly to 13 m/s then saturate. The 37.0-GHz fourth stokes second harmonic increases below 5 m/s and is observed to peak at 8 m/s, at which point it rapidly begins to decrease with wind speed. The behavior of the GMF noted here is generally consistent with previous aircraft observations at common frequencies and polarizations and it provides new constraints on the behavior of the model at other channels [2].

IV. Wind Vector Retrieval

The wind vector retrieval algorithm identifies the wind speed and direction that minimize the RMS difference between the measured surface emissivity and the empirical model functions derived above. This is equivalent to a minimization of the cost function

$$\Phi\left(\mathrm{WS}, \phi\right) = \mathrm{SST} * \left\{ \sum_f \sum_p \left(w_{f,p}\left[\varepsilon_{f,p} - \mathrm{GMF}(f, p, \mathrm{WS}, \phi)\right]\right)^2 \right\}^{1/2} \quad (8)$$

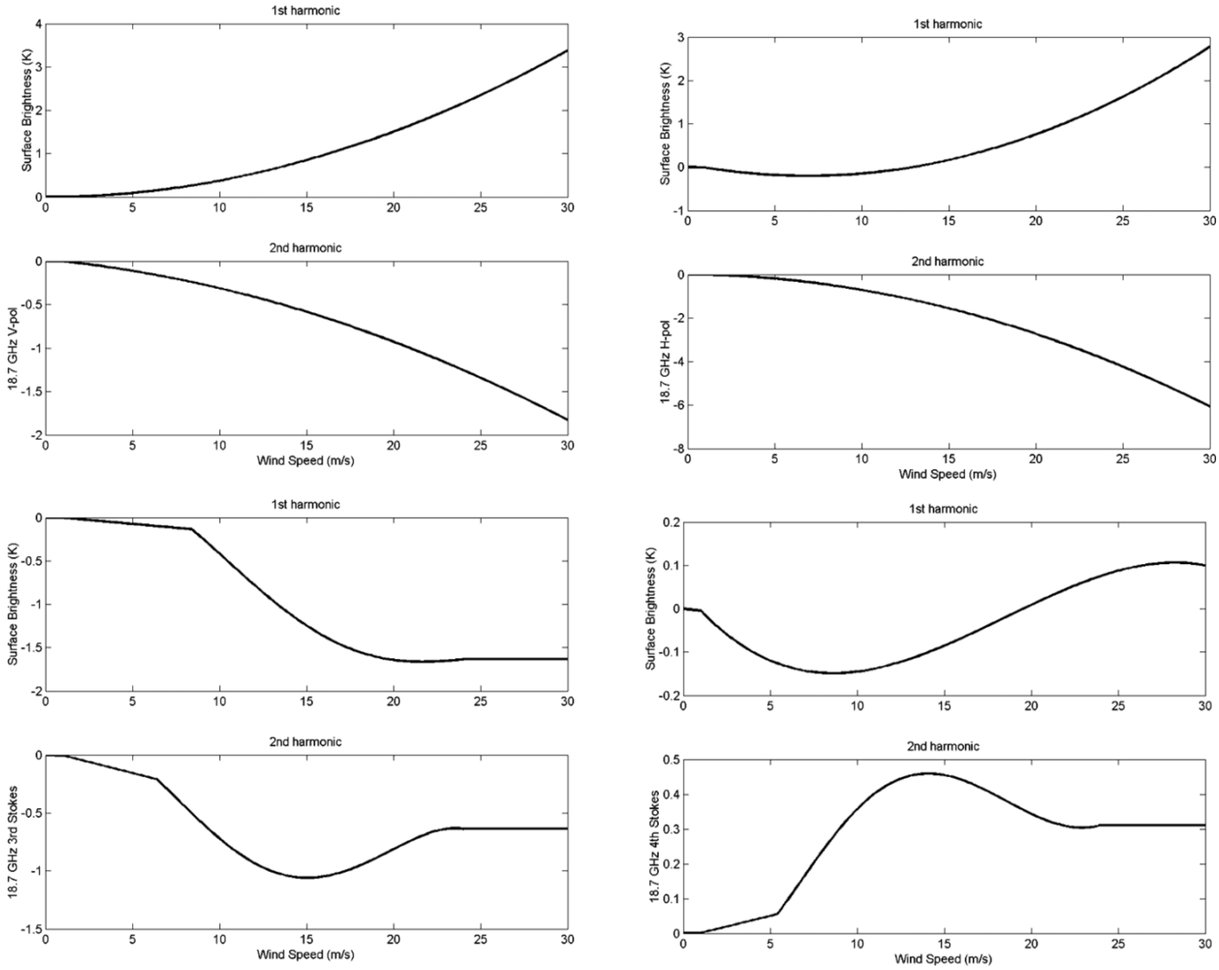

Fig. 5. The 18.7-GHz V (top left), H (top right), third (bottom left), and fourth (bottom right) Stokes first and second harmonic coefficients estimated from WindSat scaled to surface brightness ($\varepsilon * 290$) (K). The coefficients are interpolated/extrapolated from the WindSat data, shown for the third and fourth stokes in Fig. 2.

where f is frequency, p is polarization, and $w_{f,p}$ are normalized weights for each channel and the equation is scaled by the surface temperature (SST). The atmospheric clearing algorithm described in Section II is used to estimate the surface emissivity from each WindSat channel. In this initial version of the wind vector retrieval, the algorithm to determine V and L is detached from the inversion algorithm to estimate the surface wind vector. That is, the surface emissivity model and wind speed estimated in the atmospheric clearing algorithm are not used in the subsequent processing to determine the wind vector. Future work will fully couple the algorithm to estimate the atmospheric parameters with that which estimates the wind vector from the emissivity.

Because the wind vector solution is not unique (Φ can have many local minima), a search is required to locate all the minima and rank the solutions in terms of residual error. The wind vector solution with the lowest RMS difference between the measurements and model is defined as the first-rank solution. Ideally, one should employ a two-dimensional (2-D) search over wind speed and direction. This is accomplished with a brute-force searching algorithm. The algorithm forms a 2-D surface of Φ evaluated over wind speeds of 0–30 m/s in 0.1-m/s steps and 0° to 359° in 1° steps. This is illustrated in Fig. 7 in terms of surface brightness, for equal channel weighting. In this example, three minima are observed giving three solutions, which is further illustrated in a line plot of the error surface at a wind speed of 15.8 m/s, Fig. 8. The wind vector solutions are 14.9 m/s at 26.0°, 15.8 m/s at 62.0°, and 16.6 m/s at 200.0°. A coincident QuikSCAT measurement gives a wind speed of 15.4 m/s at 51.5°. The first-rank solution in this example is 15.8 m/s at 62°, which has a weighted RMS error of 0.0754 K. While it is most desirable to use the 2-D search algorithm, the processing time it required prohibited its use for operational data production. Therefore, a one-dimensional (1-D) version of the algorithm was developed.

The 1-D algorithm first determines an initial estimate of the wind speed by minimizing the RMS difference between the 10.7- and 18.7-GHz horizontally polarized emissivity measurements and the zeroth-order harmonic of the model function, (7). A 1-D search of Φ over wind direction fixed at the initial wind speed is then conducted to find the wind direction solutions. The channel weighting, $w_{f,p}$ in (8), for the 1-D search is 0.22 for the 10.7-GHz third and fourth Stokes, 0.17 for the 18.7-GHz third and fourth Stokes and 0.11 for the 37.0-GHz third and fourth Stokes. The values for these weights were determined in an *ad hoc* manner so as to optimize the retrieval of wind vector by the algorithm. No weight is given to the V- and H- pol channels for the 1-D search over wind direction. The additional

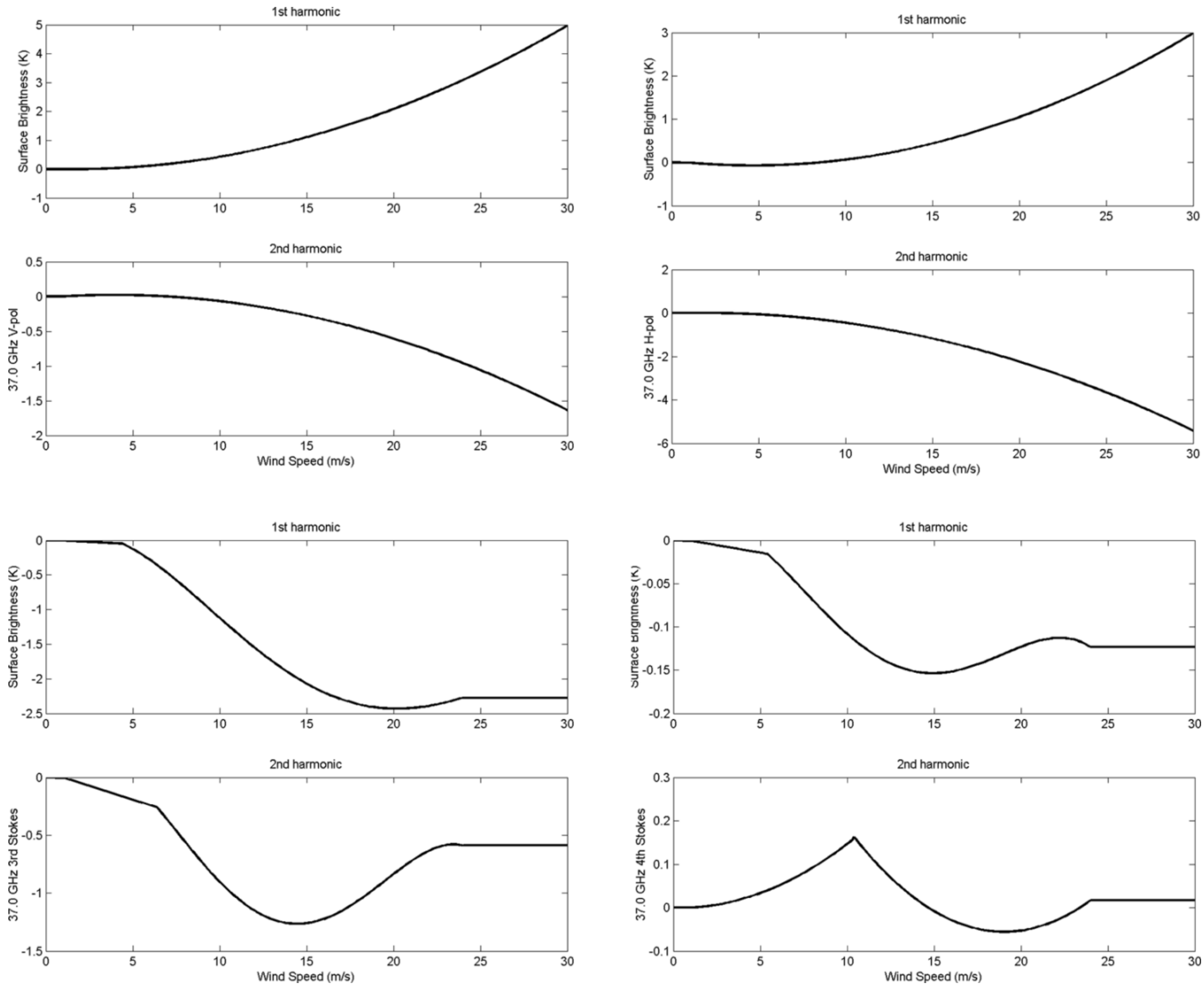

Fig. 6. The 37.0-GHz V (top left), H (top right), third (bottom left), and fourth (bottom right) Stokes first and second harmonic coefficients estimated from WindSat scaled to surface brightness ($\varepsilon * 290$) (K). The coefficients are interpolated/extrapolated from the WindSat data, shown for the third and fourth stokes in Fig. 3.

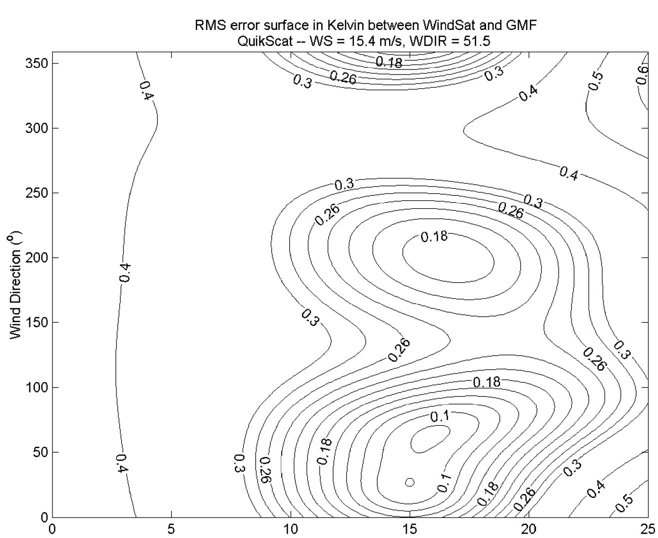

Fig. 7. Two-dimensional surface of RMS difference (in Kelvin) between WindSat and the Model function evaluated over wind speed and direction. A colocated QuikSCAT measurement gives a wind speed of 15.4 m/s and direction of 51.5°. There are three solutions in this example.

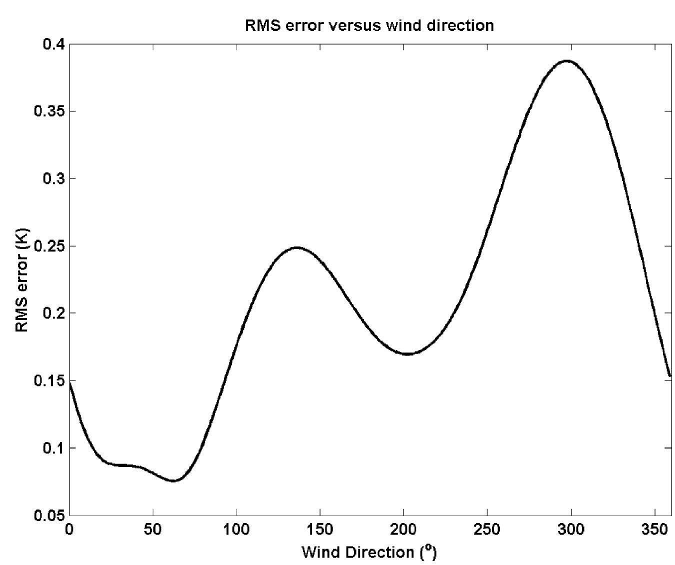

Fig. 8. Line plot of the 2-D surface in Fig. 7 at a wind speed of 15.8 m/s. In this example, the first-rank solution is the closest to the QuikSCAT measurement.

noise in the emissivity estimate for the V- and H-pol channels due to imperfect atmospheric clearing caused the wind direction retrieval accuracy to degrade slightly as compared to using only the polarimetric channels. It is believed that the residual atmospheric effect in the V- and H-pol emissivities can be reduced by coupling the atmospheric and wind vector inversion

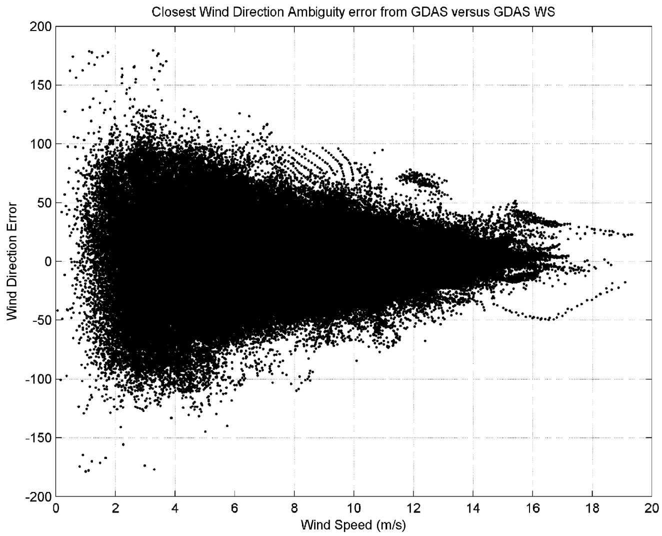

Fig. 9. Closest wind direction ambiguity error from GDAS model outputs versus wind speed.

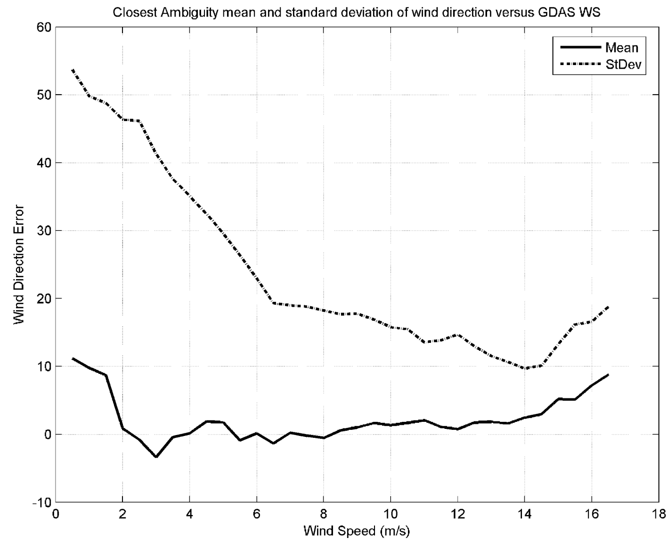

Fig. 10. Mean and standard deviation of the closest wind direction ambiguity error from GDAS versus wind speed.

algorithms. A final refinement is made to the wind speed estimate for each wind direction solution by fixing the wind direction found in the second step and finding that wind speed which minimizes Φ. The channel weighting for the wind speed refinement is 0.104 for the 10.7-, 18.7-, and 37.0-GHz V- and H-pol channels and 0.0625 for the 10.7-, 18.7-, and 37.0-GHz third and fourth Stokes channels. The wind vector solutions are then ranked in order of lowest residual error.

V. Algorithm Performance

The performance of the wind retrieval algorithm is assessed by evaluating its performance against colocated GDAS wind vector outputs. Only the outputs that were within ± 3 h of the WindSat measurement were included. The colocated data were also required to be within 60 min of a QuikSCAT measurement and 35 min of a SSM/I measurement, although these data are not used in the subsequent analysis. The purpose for this was to reduce the size the of the colocated dataset for computational purposes and to generate a more detailed matched dataset for future analysis. The GDAS data subset consisted of approximately 425 000 globally distributed points covering a wide range of water vapor, cloud liquid water, SST, and wind speed values taken over a four month time span from September to December of 2003. Fig. 9 shows the difference of the wind direction retrieval from the coincident GDAS output and Fig. 10 shows the mean and standard deviation of the wind direction error in 2-m/s bins. The solution used in the analysis is the closest wind direction ambiguity, which is defined as the ambiguity that is closest to the model output. Therefore, these results show the best possible performance of the algorithm (i.e., the performance if an ambiguity selection algorithm is used that always picks the most accurate solution). One measure of the algorithm's ability to select the correct ambiguous solution is termed its skill, which is defined as the percentage of cases in which the first-rank solution is the closest wind direction ambiguity. The skill is shown in Fig. 11. The skill is very high above 10 m/s, greater than 85%, and it is 90% at 15 m/s. The skill is 75% at 7 m/s and

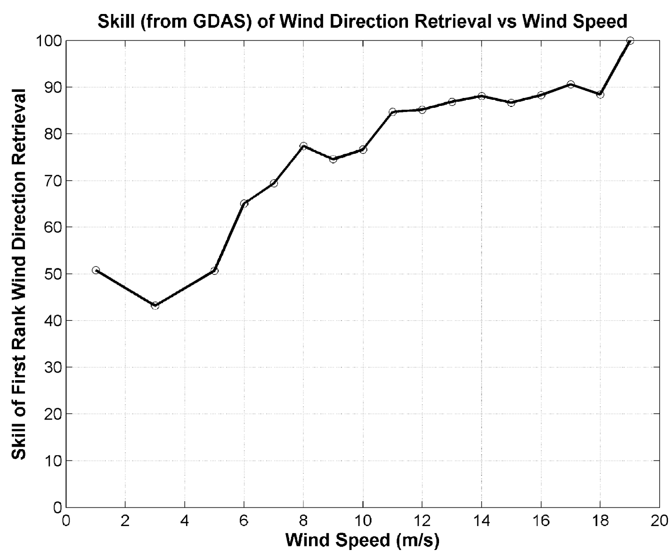

Fig. 11. Skill of the wind direction retrieval algorithm. Skill is defined as the percentage of first-rank solutions that are the closest wind direction ambiguity.

less than 50% for wind speeds less than 5 m/s. The RMS error of wind direction decreases with increasing wind speed because the strength of the emission signal becomes much greater than the noise floor of the emissivity retrieval. The standard deviation of the closest wind direction ambiguity is less than 20° for wind speeds greater than 6 m/s and less than 15° for wind speeds greater than 10 m/s. Some other more sophisticated ambiguity selection algorithm, such as a median filter, is required to further improve the algorithm's ability to return the solution that is closest to the true wind direction. It should be noted that the standard deviations quoted here include errors from both GDAS and WindSat. Therefore, these error statistics represent an upper bound on the algorithm's performance. A detailed error budget is beyond the scope of this paper.

The performance of the algorithm in the absence of an ambiguity selection algorithm (i.e., performance lower bound) is assessed in Fig. 12 which shows histograms of the error in the first-

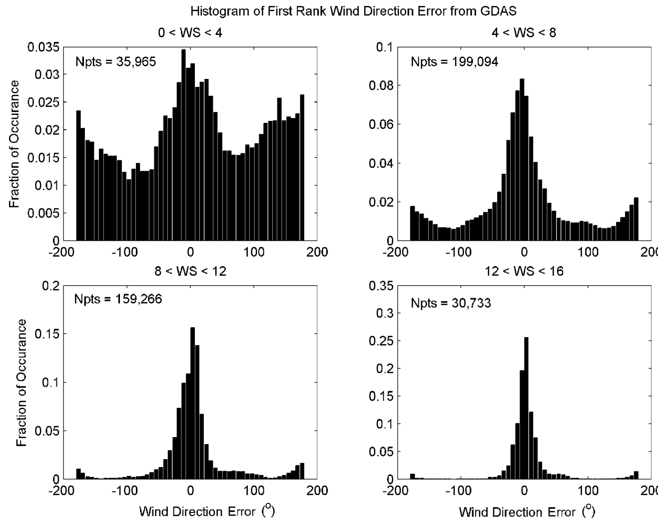

Fig. 12. Histogram of first-rank wind direction error from GDAS grouped into four wind speed bins.

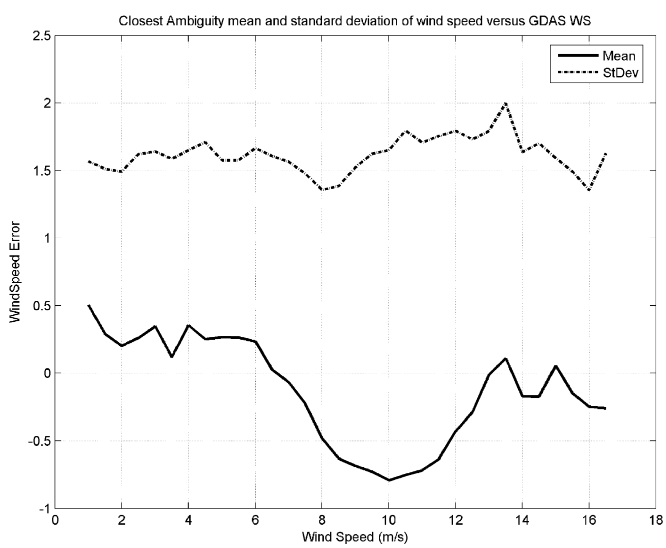

Fig. 13. Mean and standard deviation of the wind speed retrieval error compared to GDAS versus wind speed.

rank solution grouped into four wind speed bins. The number of ambiguous solutions was generally evenly distributed between two and three and relatively independent of wind speed. The solution with the lowest RMS residual is the first-rank solution. For wind speeds less than 4 m/s, there is a poorly defined peak near zero bias and the wind direction retrieval error is widely distributed. As the wind speed (and likewise the retrieval skill) increases, the peak around zero bias narrows and becomes more defined, with many fewer first-rank solutions having large errors. Above 12 m/s, almost all of the first-rank solutions are grouped in a Gaussian-like distribution centered at zero bias. This is consistent with the high retrieval skill at these wind speeds.

The performance of the wind speed retrieval is shown in Fig. 13. The standard deviation of the wind speed retrieval error from GDAS is approximately 1.5 m/s for wind speeds less than 17 m/s. The wind speed and direction comparison statistics above 17 m/s are not reliable due to an insufficient amount of matched data and are therefore not included in Figs. 10–13.

VI. Conclusion

A wind vector retrieval algorithm for the WindSat polarimetric radiometer is developed. The surface emissivity is estimated at each WindSat channel using an atmospheric clearing algorithm developed for this study. An empirical geophysical model function relating the surface emissivity to the wind vector is derived. An even and odd Fourier expansion is used to represent the functional dependence of the emissivity on wind direction where the harmonic coefficients are determined from colocated QuikSCAT wind vector measurements. The observed dependence of the harmonic coefficients on wind speed is consistent with coefficients determined from aircraft observations and additionally provide observations over a larger range of wind speed. The confidence in the derived harmonics for the polarimetric channels is high and should be considered suitable to validate analytical surface scattering models for polarized ocean surface emission.

The performance of the retrieval algorithm was assessed using comparisons to GDAS wind vector outputs. The wind speed was retrieved with an RMS uncertainty of 1.5 m/s. The RMS uncertainty of the closest wind direction ambiguity is less than 20° for wind speeds greater than 6 m/s and less than 15° at 10 m/s. The retrieval skill, the percentage of retrievals in which the first-rank solution is the closest wind direction ambiguity, was 75% at 7 m/s and 85% above 10 m/s. An ambiguity removal algorithm, such as a median filter, can be applied to the retrievals to further increase the percentage of selected solutions that are the closest wind direction ambiguity.

Several limitations of the retrieval algorithm were addressed which will be the subject of future investigation. Sea foam was not included in the model used to determine the specular reflectivity correction factor, Ω, and the effect of this on the retrieval algorithm at high wind speeds should be investigated. Furthermore, a thorough investigation of the variation of Ω on wind speed and direction is advised in order to improve the simple linear dependence on wind speed used in this study. In the present algorithm, the atmospheric inversion and wind vector inversion algorithms are decoupled. Future improvements to the retrieval algorithm will simultaneously solve for the atmospheric and wind vector inversion algorithm in order to produce more accurate estimates of each. Additional work can be done to find the optimal set of channel weights in (8) which will produce the best estimate of the wind vector given a set of WindSat emissivity estimates. The channel weights should reflect the signal strength of a particular channel and the confidence in the derived model function for that channel.

References

[1] S. Yueh, W. Wilson, F. Nghiem, and W. Ricketts, "Polarimetric measurements of sea surface brightness temperatures using an aircraft K-band radiometer," *IEEE Trans. Geosci. Remote Sens.*, vol. 33, no. 1, pp. 85–92, Jan. 1995.

[2] S. Yueh, W. Wilson, S. Dinardo, and F. Li, "Polarimetric microwave brightness signatures of ocean wind directions," *IEEE. Trans. Geosci. Remote Sens.*, vol. 37, no. 2, pp. 949–959, Mar. 1999.

[3] J. Piepmeier and A. Gasiewski, "High-resolution passive polarimetric microwave mapping of the ocean surface wind vector fields," *IEEE Trans. Geosci. Remote Sens.*, vol. 39, no. 3, pp. 606–622, Mar. 2001.
[4] P. Gaiser *et al.*, "The WindSat spaceborne polarimetric microwave radiometer: Sensor description and early orbit performance," *IEEE Trans. Geosci. Remote Sens.*, vol. 42, no. 11, pp. 2347–2361, Nov. 2004.
[5] L. Tsang, J. Kong, and R. Shin, *Theory of Microwave Remote Sensing*. New York: Wiley, 1985.
[6] S. Yueh, "Modeling of wind direction signals in polarimetric sea surface brightness temperatures," *IEEE Trans. Geosci. Remote Sens.*, vol. 35, no. 6, pp. 1400–1417, Nov. 1997.
[7] M. Zhang and J. Johnson, "Comparison of modeled and measured second azimuthal harmonics of ocean surface brightness temperatures," *IEEE Trans. Geosci. Remote Sens.*, vol. 39, no. 2, pp. 448–452, Feb. 2001.
[8] J. T. Johnson and Y. Cai, "A theoretical study of sea surface up/down wind brightness temperature differences," *IEEE Trans. Geosci. Remote Sens.*, vol. 40, no. 1, pp. 66–78, Jan. 2002.
[9] U. F. R. Moore and A. Fung, *Microwave Remote Sensing: Active and Passive*. Canton, MA: Artech House, 1981, vol. I, ch. 5.
[10] F. Wentz, "A well-calibrated ocean algorithm for Special Sensor Microwave/Imager," *J. Geophys. Res.*, vol. 102, no. C4, pp. 8703–8718, 1997.
[11] P. Rosenkranz, "Absorption of microwaves by atmospheric gases," in *Atmospheric Remote Sensing by Microwave Radiometry*, M. A. Janssen, Ed. New York: Wiley, 1993, ch. 2.
[12] Cruz-Pol, R. C. Ruf, and S. Keihm, "Improved 20–32 GHz atmospheric absorption model," *Radio Sci.*, vol. 22, no. 5, pp. 1319–1333, 1998.
[13] Walcek and Taylor, "A theoretical method for computing vertical distributions of acidity and sulfate production within cumulus clouds," *J. Atmos. Soc.*, vol. 43, pp. 339–355, 1986.
[14] A. Benoit, "Signal attenuation due to neutral oxygen and water vapor, rain and clouds," *Microw. J.*, vol. 11, pp. 73–80, 1968.
[15] L. A. Klein and C. T. Swift, "An improved model for the dielectric constant of sea water at microwave frequencies," *IEEE Trans. Antennas Propogat.*, vol. AP-25, pp. 104–111, 1976.
[16] P. C Pandey and R. K. Kakar, "An empirical microwave emissivity model for a foam-covered sea," *IEEE J. Oceanic Eng.*, vol. OE-7, no. 3, pp. 135–140, 1982.
[17] S. Levitus, R. Burgett, and T. P. Boyer, *World Ocean Atlas 1994*. Silver Spring, MD: NOAA NESDIS, 1994, vol. 3, Salinity, p. 111. NOAA Atlas NESDIS 3.
[18] C. Rodgers, *Inverse Methods for Atmospheric Sounding: Theory and Practice*, Singapore: World Scientific, 2000, pp. 81–86.
[19] S. Wu and A. Fung, "A noncoherent model for microwave emissions and backscattering from the sea surface," *J. Geophys. Res.*, vol. 77, no. 30, pp. 5917–5929, 1972.
[20] S. Yueh, R. Kwok, F. Li, S. Nghiem, W. Wilson, and J. Kong, "Polarimetric passive remote sensing of random discrete scatterers and rough surfaces," *Radio Sci.*, pp. 799–814, 1994.
[21] F. Wentz, "A model function for ocean microwave brightness temperatures," *J. Geophys. Res.*, vol. 88, pp. 1892–1908, 1983.
[22] D. R. Lyzenga, "Comparison of WindSat brightness temperatures with two-scale model predictions," *IEEE Trans. Geosci. Remote Sens.*, no. 3, pp. 549–559, Mar. 2006.

Shannon T. Brown (S'02–M'05) received the B.S. degree in meteorology from Pennsylvania State University, University Park, and the M.S. degree in atmospheric science and the Ph.D. degree in geoscience and remote sensing from the University of Michigan, Ann Arbor, in 2001, 2003, and 2005, respectively.

He is a member of the engineering staff in the Microwave Advanced Systems Section, NASA Jet Propulsion Laboratory, Pasadena, CA. His research interests involve on-orbit calibration/validation and performance assessment of the Jason Microwave Radiometer and of the WindSat polarimetric microwave radiometer, development of an on-Earth hot calibration brightness temperature reference for satellite microwave radiometers, surface wind speed and rain rate retrieval algorithm development using airborne active and passive microwave measurements in rain, and development of a wind vector retrieval algorithm from space using the WindSat polarimetric microwave radiometer.

Dr. Brown is the recipient of a 2004 NASA Group Achievement Award for his contribution to the UMich/GSFC Lightweight Rainfall Radiometer.

Christopher S. Ruf (S'85–M'87–SM'92–F'01) received the B.A. degree in physics from Reed College, Portland, OR, and the Ph.D. degree in electrical and computer engineering from the University of Massachusetts, Amherst.

He is currently a Professor of atmospheric, oceanic, and space sciences and electrical engineering and computer science at the University of Michigan, Ann Arbor. He has worked previously as a Production Engineer for Intel Corporation, Santa Clara, CA, as a member of the technical staff for the Jet Propulsion Laboratory, Pasadena, CA, and as a member of the faculty at Pennsylvania State University, University Park. During 2000, he was a Guest Professor at the Technical University of Denmark, Lyngby. His research interests involve microwave remote sensing instrumentation and geophysical retrieval algorithms. He is currently involved with spaceborne radiometers on the current TOPEX, GeoSat Follow-on, Jason, and WindSat and the upcoming CMIS, Aquarius, and Juno missions. He has published over 87 refereed articles and is a past Associate Editor and Guest Editor for *Radio Science*.

Dr. Ruf has received three NASA Certificates of Recognition and four NASA Group Achievement Awards, as well as the 1997 GRS-S Transactions Prize Paper Award and the 1999 IEEE Judith A. Resnik Technical Field Award. He is a past Editor of the IEEE GRS-S Newsletter and currently an Associate Editor and Guest Editor of the IEEE TRANSACTIONS ON GEOSCIENCE AND REMOTE SENSING. He is a member of the AGU, AMS, and URSI Commission F.

David R. Lyzenga received the B.S.E. degree in engineering physics from the University of Michigan, Ann Arbor, the M.S. degree in physics from Yale University, New Haven, CT, and the Ph.D. degree in electrical engineering from the University of Michigan, in 1967, 1968, and 1973, respectively.

He worked at the Environmental Research Institute of Michigan from 1974 to 1987, and was an Associate Professor in the College of Marine Studies, University of Delaware from 1987 to 1989. He presently holds joint research appointments at the University of Michigan and the General Dynamics Advanced Information Systems Division, Ann Arbor. His research interests include interactions of electromagnetic radiation with the ocean, and remote sensing of the ocean using both radar and optical techniques.